A numerical investigation of the flow in the wicket gate and runner of the Hölleforsen (Turbine 99) Kaplan turbine model

H. Nilsson* and L. Davidson†

Abstract

The Hölleforsen Kaplan model draft tube was thoroughly investigated at the *Turbine 99* workshop on draft tube flow [1, 3], in 1999. The velocity distribution measured close to the runner blade suction side was used as an inlet boundary condition for the *Turbine 99* contributions and the remainder of the measurements were used for validation of the draft tube computational results. It was found at the workshop that the lack of an inlet radial velocity distribution had a drastic effect on the computational results in the draft tube. Some of the contributions assumed a radial velocity distribution that aligned the flow with the walls at the inlet, while other contributions assumed a zero radial velocity component at the inlet. The lack of a draft tube inlet radial velocity distribution was caused by restrictions on the visual access in the model.

This work numerically studies the flow in the wicket gate and runner of the Hölleforsen turbine model. The computations are made in two steps. The flow in the wicket gate is first computed. The flow is assumed to be steady and periodic, so that only one blade passage must be computed. The wicket gate computation shows good agreement with observations. The result of this computation is circumferentially averaged and applied as boundary conditions for the stationary periodic runner computations. The runner computational results show good agreement with the *Turbine 99* measurements at the draft tube inlet, and a comparison between the assumed radial velocity distribution for the *Turbine 99 - II* workshop and the computations is made.

A thorough investigation of the computed flow in the wicket gate and runner of the Hölleforsen turbine model is presented.

1 Introduction

At the *Turbine 99* workshop, it was found that the inlet boundary conditions had a drastic influence on the computational results in the draft tube. The measurements provided at the draft tube inlet lacked the radial velocity component and detailed turbulent quantities. Owing to restrictions on the measurement technique, information on the flow in the boundary layers close to the hub and shroud was partly missing. The organizers of the workshop decided that it should be up to the contributors to fill in the missing information, as an interesting topic for discussion at the workshop and as a source of differences in the solutions. It was found that the differences in the assumptions made by the contributors had a huge effect on the computational results and similar computations made by different contributors resulted in completely different flow fields. The differences were believed to originate in differences in the inlet conditions and grid properties. For the follow-up workshop, *Turbine 99 - II*, the organizers decided to make a common case, where the missing information is modeled using simple relations and a multiblock grid that should be used by all the contributors is available.

The flow at the inlet to the draft tube is highly dependent on the flow in the runner. Computational results that match the available measurements at the draft tube inlet thus reveal most of the missing information. In this work, the CALC-PMB [6, 12, 14, 15] parallel multiblock finite volume CFD (Computational Fluid Dynamics) code for computations of turbulent flow in complex domains is used for computations of the flow in the Hölleforsen Kaplan turbine model. The computations include both the guide vanes and the runner, where the runner computations receive the inlet conditions from the guide vane computations.

The model runner has a diameter of $0.5m$. It has five runner blades and 24 guide vanes. The tip clearance between the runner blades and the shroud is $0.4mm$. The computations are made at a head of $H = 4.5m$, a runner speed of $N = 595rpm$ and a volume flow of $Q = 0.522m^3/s$. This operating condition is close to the best efficiency operating point, at 60% load, and it was referred to as test case T (top point of the propeller curve) at the *Turbine 99* workshop. The head of the real power plant, which is situated in Indalsälven in Sweden, is $27m$ and consists of three Kaplan turbines with a runner diameter of $5.5m$, maximum power of $50MW$ and flow capacity of $230m^3/s$ per turbine.

2 Numerical considerations

The main features of the CALC-PMB CFD code are its use of conformal block structured boundary fitted coordinates, a pressure correction scheme (SIMPLEC [7]), cartesian velocity components as the principal unknowns, and a collocated grid arrangement together with Rhie and Chow interpolation. The discretization schemes used in this work are a second-order Van Leer scheme for convection and

*CHALMERS, Dept. of Thermo and Fluid Dynamics, SE - 412 96 Gothenburg, hani@tfd.chalmers.se, http://www.tfd.chalmers.se/∼hani

†CHALMERS, Dept. of Thermo and Fluid Dynamics, SE - 412 96 Gothenburg, lada@tfd.chalmers.se, http://www.tfd.chalmers.se/∼lada

a second-order central scheme for the other terms. The computational blocks are solved in parallel with Dirichlet-Dirichlet coupling using PVM (Parallel Virtual Machine) or MPI (Message Passing Interface). The parallel efficiency is excellent, with super scalar speedup for load balanced applications [12, 14]. The ICEM CFD/CAE grid generator is used for grid generation and Ensight and Matlab are used for post-processing.

The computations include both the guide vanes and the runner. Since the computations involve rotating and stationary frames of references, the interaction between these is numerically very complicated. A simple approach is used in this work where the computations are made in two steps. The stationary guide vanes are first computed without the runner blades. The runner is then computed, using the circumferentially averaged velocities and turbulent quantities from the guide vane computations after the guide vanes. The upstream effect of the runner blades on the flow at the guide vanes is neglected because of computational restrictions and measurements that reveal no upstream effects of the runner blades on the velocities at the guide vanes [13]. The computations of both the guide vanes and the runner are confined to a single guide vane or runner blade. This includes no extra restrictions since the boundary conditions are assumed to be stationary axisymmetric, and the stationary Reynolds averaged solution is thus periodic.

A low Reynolds number turbulence model is used to resolve the turbulent flow in the tip clearance and the boundary layers. Since part of the computational domain is rotating, Coriolis and centripetal effects are included in the momentum equations. The $k-\omega$ turbulence model of Wilcox [18], which can be integrated all the way to the wall, is used without terms for rotational effects. This is common in turbomachinery computations for reasons of numerical stability and the small impact of such terms in these kinds of industrial applications. Because of computational restrictions, complete turbine simulations found in the literature usually use wall functions instead of resolving the boundary layers, which makes tip clearance investigations impossible. To keep the grid size as small as possible and the control volumes as orthogonal as possible, the computational grid is created in a multiblock topology using ICEM CFD/CAE. During the computations, the computational blocks are assigned to separate PVM or MPI processes. The level of parallelization is thus determined by the block size distribution and the distribution of the processes on the available processors.

The correct solution is assumed to be reached when the largest normalized residual of the momentum equations, the continuity equation and the turbulence equations are reduced to 10^{-3} [12]. The momentum equation residuals are normalized by the sum of the mass flow through the turbine and the mass flow through the periodic surfaces multiplied by the largest value of the velocity component of each equation. The continuity equation residual is normalized by the sum of the mass flow through the turbine and the mass flow through the periodic surfaces. The turbulence equations residuals are normalized by the largest residual during the iterations.

Apart from the validation against measurements in this work, the computational technique has been extensively validated against the GAMM Francis runner [17] and academic test cases [12, 15].

2.1 Equations

The equations used for the computations are briefly described below.

The stationary Reynolds time-averaged continuity and Navier Stokes equations for incompressible flow in a rotating frame of reference read [5, 10]

$$\frac{\partial \rho U_i}{\partial x_i} = 0$$

$$\begin{aligned}\frac{\partial \rho U_i U_j}{\partial x_j} = & - \frac{\partial P}{\partial x_i} + \frac{\partial}{\partial x_j}\left((\mu+\mu_t)\frac{\partial U_i}{\partial x_j}\right) + \rho g_i \\ & - \rho\epsilon_{ijk}\epsilon_{klm}\Omega_j\Omega_l x_m - 2\rho\epsilon_{ijk}\Omega_j U_k\end{aligned}$$

where $-\epsilon_{ijk}\epsilon_{klm}\Omega_j\Omega_l x_m$ is the centripetal term and $-2\epsilon_{ijk}\Omega_j U_k$ is the Coriolis term, owing to the rotating coordinate system. Because of the potential nature of the pressure, gravitational and centripetal terms [10], they are put together during the computations in what is often referred to as a *reduced* pressure gradient

$$-\frac{\partial P^*}{\partial x_i} = -\frac{\partial P}{\partial x_i} + \rho g_i - \rho\epsilon_{ijk}\epsilon_{klm}\Omega_j\Omega_l x_m$$

Thus, a relation for the *reduced* pressure is

$$P^* = P - \rho g_i x_i + \rho\epsilon_{ijk}\epsilon_{klm}\Omega_j\Omega_l x_m x_i$$

In post-processing, the variation of the gravity term is assumed to be negligible and the centripetal term is simply subtracted from the *reduced* pressure.

The $k-\omega$ model of Wilcox [18] for the turbulent kinetic energy, k, and the specific dissipation rate, ω, reads

$$\begin{aligned}\frac{\partial \rho U_j k}{\partial x_j} &= \frac{\partial}{\partial x_j}\left[\left(\mu+\frac{\mu_t}{\sigma_k}\right)\frac{\partial k}{\partial x_j}\right] \\ &+ P_k - \rho\beta^\star\omega k \\ \frac{\partial \rho U_j \omega}{\partial x_j} &= \frac{\partial}{\partial x_j}\left[\left(\mu+\frac{\mu_t}{\sigma_\omega}\right)\frac{\partial \omega}{\partial x_j}\right] \\ &+ \frac{\omega}{k}\left(c_{\omega 1}P_k - c_{\omega 2}\rho k\omega\right)\end{aligned}$$

where the turbulent viscosity, μ_t, is defined as

$$\mu_t = \rho\frac{k}{\omega}$$

The production term reads

$$P_k = \mu_t\left(\frac{\partial U_i}{\partial x_j} + \frac{\partial U_j}{\partial x_i}\right)\frac{\partial U_i}{\partial x_j}$$

and the closure coefficients are given by

$$\beta^\star = 0.09,\ c_{\omega 1} = \tfrac{5}{9},\ c_{\omega 2} = \tfrac{3}{40},\ \sigma_k = 2 \text{ and } \sigma_\omega = 2$$

At the walls, a no-slip condition is applied for the velocities, $k = 0$ and at the first node normal to the wall (at $y^+ < 2.5$) $\omega = 6\nu/(C_{\omega 2}n^2)$ where n denotes the normal distance to the wall. For the pressure, $\partial^2 P/\partial n^2 = 0$ at all boundaries.

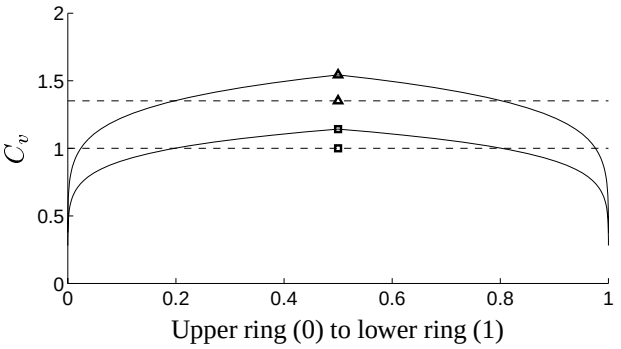

Figure 2.1: Inlet boundary conditions for the guide vane computations. Solid lines: 1/7 profile inlet; dashed lines: uniform inlet. Markers: △: tangential; □: meridional.

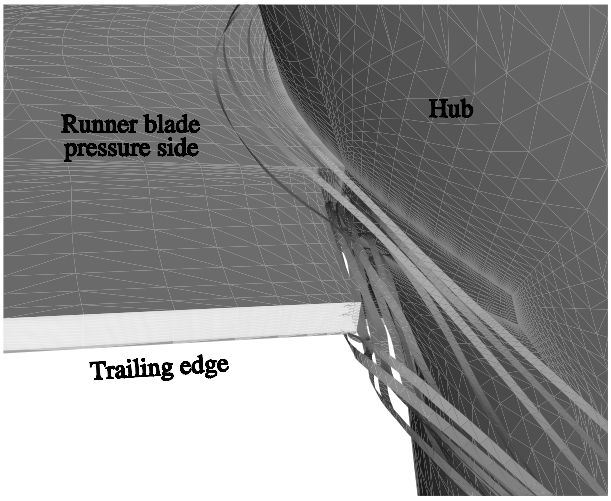

Figure 2.2: The hub clearance is included in some of the computations. In this zoom-up of the hub clearance region, some stream ribbons that pass through the hub clearance are visualized. The stream ribbons originate both from the pressure and suction sides of the blade.

2.2 Guide vane computations

The inlet boundary condition should be moved as far away from the investigated section as possible in order to reduce the effects of the inlet boundary. Since the guide vanes are located very close to the runner, it is necessary to include them in the computations. It is also desirable to include the spiral casing and part of the penstock in the computations. The inclusion of the spiral casing would however introduce a variation in volume flow at different circumferential positions. It would thus not be possible to employ periodic boundary conditions, and the total grid size for the guide vane and runner computations would grow to $10\,440\,403$ control volumes with the present resolution.

The flow in the guide vane passages is computed under stationary and periodic assumptions. The grid for a single guide vane passage consists of $285\,177$ control volumes, which is found to be sufficient to resolve the circumferentially averaged flow at the inlet of the runner computations. The clearance between the trailing edge of the guide vanes and the shroud, owing to the curvature of the meridional contour of the shroud, is not included in the computations. The guide vane angle of the studied operating condition is 27.5^o, measured from the closed position, which is at an angle of 9^o from the tangential direction.

Since the flow in the spiral casing is not included in the computations (see figure 2.3), the flow at the inlet of the guide vane computations is assumed to be aligned with the guide vanes. Two different approaches to specify the inlet boundary condition are compared, a uniform velocity distribution and a fully developed turbulent 1/7 profile [6, 12]. The inlet boundary conditions are shown in figure 2.1. The inlet boundary conditions are constant in the circumferential direction, and the flow is aligned with the guide vanes.

The inlet turbulent kinetic energy is estimated by

$$k_{in} = C_\mu^{-0.5} l_m^2 \left(\frac{\partial U}{\partial y}\right)^2$$

where l_m is the Prandtl's mixing length and is given by

$$l_m = \min(\kappa y, \lambda\delta)$$

where $\kappa = 0.41$ is the von Karman constant, $\lambda = 0.09$, y is the distance from the wall and δ is the inlet height. This relation stems from the assumption of turbulence-energy equilibrium, i.e. production of turbulent kinetic energy is balanced by its dissipation. The inlet specific dissipation is set according to

$$\omega_{in} = \frac{\rho k_{in}}{10\mu}$$

The computational domain includes the runner section, but the runner is not included in the computations. At the outlet, fully developed Neumann boundary conditions [12] are used. The computations are made for a single guide vane using axisymmetric inlet boundary conditions and assuming stationary periodic flow. The purpose of the guide vane computations is to generate inlet boundary conditions for the runner computations.

2.3 Runner computations

The flow in the runner blade passages is computed under stationary and periodic assumptions, relative to the rotating coordinate system. The grid for a single runner blade passage consists of $719\,231$ control volumes. $15\,884$ control volumes are in the tip clearance, where 19 control volumes are in the runner blade tip to shroud direction. For computations including the clearance at the trailing edge close to the hub (see figure 2.2), an extra block with $2\,926$ control volumes was used. The inclusion of the hub clearance introduced extra convergence problems, since it was not affordable to resolve the boundary layers properly. However, comparisons with computational results using a grid that was not prepared for hub clearance inclusion showed that this did not affect the overall results. It is however questionable whether the flow in the hub clearance is properly modeled.

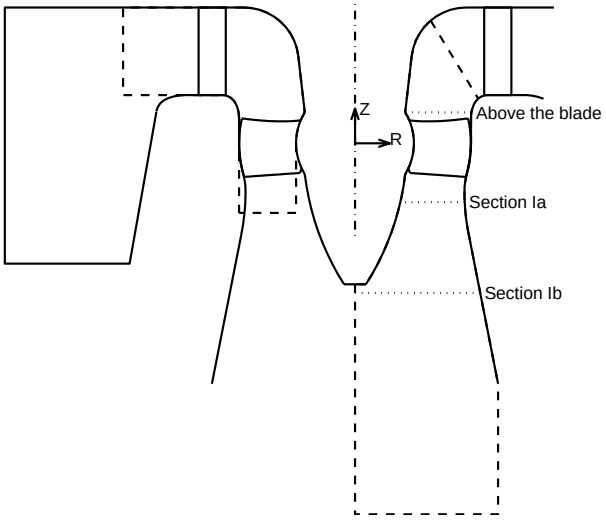

Figure 2.3: The meridional contour (including runner blades and guide vanes at the studied operating condition) of the model turbine (solid lines) and the domains that are computed (dashed lines). The left domain is the guide vane domain, with a radial inlet in the spiral casing region and an axial outlet in the runner region. The right domain is the runner domain, with a tilted inlet between the guide vanes and the runner blades and an axial outlet at the lower part of the figure. The dotted lines are sections in which the results are circumferentially averaged for post-processing. They are termed (from top) *above the blade*, *section Ia* and *section Ib*. The dashed-dotted line is the axis of rotation.

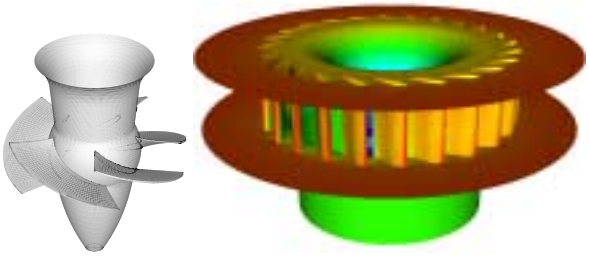

Figure 2.4: The runner and guide vane geometries.

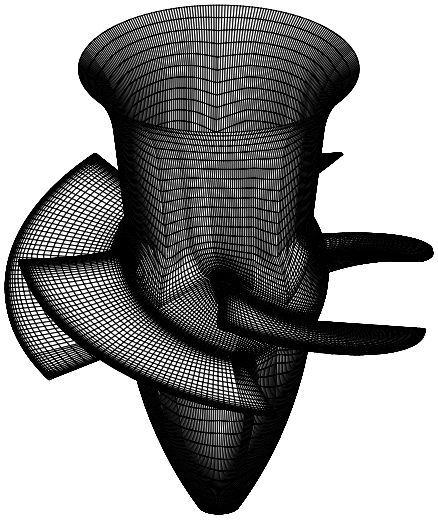

Figure 2.5: The runner grid. Note that all five blades are shown, although only one runner blade passage is computed, employing periodic boundary conditions.

The computational domain starts between the guide vanes and the runner blades (see figure 2.3), where axisymmetric inlet boundary conditions, circumferentially averaged from the guide vane computations, are applied. Fully developed Neumann boundary conditions are used at the outlet. The outlet is located after the end of the axisymmetric diffusor before the draft tube bend, with a short cylindrical section added to reduce outlet effects. Since the computations are made in a rotating frame of reference, the velocity on the rotating surfaces is set to zero while the velocity on the stationary surfaces is given a counter-rotating velocity component. The computations are made for a single runner blade assuming stationary periodic flow.

The Hölleforsen turbine model geometry used in this work is shown in figure 2.4. Note that the computations are made assuming periodic flow, so that only one blade passage must be computed. What cannot be seen in the figure is that the tip clearance is included and the clearance between the guide vanes and the shroud is excluded. The hub clearance at the trailing edge of the runner blades is included in some of the computations. The real model has no hub clearance at the leading edge of the runner blades.

Figure 2.5 shows the complicated multiblock grid used for the runner computations. The same grid is used both for computations with hub clearance and computations without hub clearance. In this way, the differences between the computational results will depend only on the hub clearance and not on node distribution effects. The hub clearance distorted the grid at the trailing edge of the runner blades somewhat and it was not affordable to resolve the hub clearance boundary layers properly. The computational results in the hub clearance can therefore only be seen as qualitative.

3 Computational results

The detailed investigations of the computational results are shown as circumferentially averaged properties at the inlet to the guide vane computations, at the inlet to the runner computations, above the runner blades, at section Ia and at section Ib (see figure 2.3). The tip clearance flow and global flow features are briefly investigated .

The velocity coefficients, C_v, are the velocities normalized by Q/A_i, where Q is the volume flow and A_i is the circumferential area of each section ($Q = 0.522m^3/s$, $A_i = 0.59m^2$ for the guide vane inlet section, $A_i = 0.27m^2$ for the interface section, $A_i = 0.16m^2$ for the section above the blades, $A_i = 0.15m^2$ for section Ia and $A_i = 0.23m^2$ for section Ib).

As at the *Turbine 99* workshop, the absolute tangential velocity is defined as positive when the flow is co-rotating with the runner, and the axial (commonly denoted as meridional) velocity is defined as positive in the main flow direction. The radial velocity is defined here as positive when the

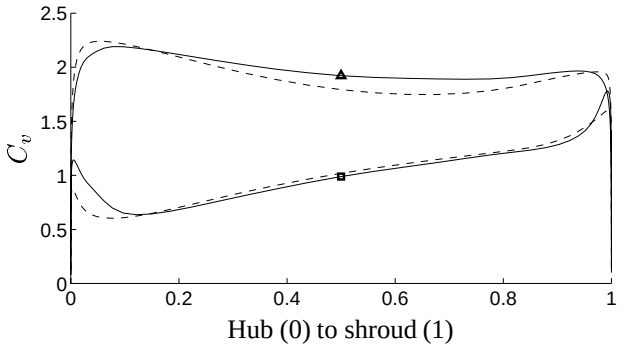

Figure 3.1: Computational results at the interface between the guide vane computations and the runner computations. Solid lines: 1/7 profile inlet; dashed lines: uniform inlet. Markers: △: tangential; □: meridional.

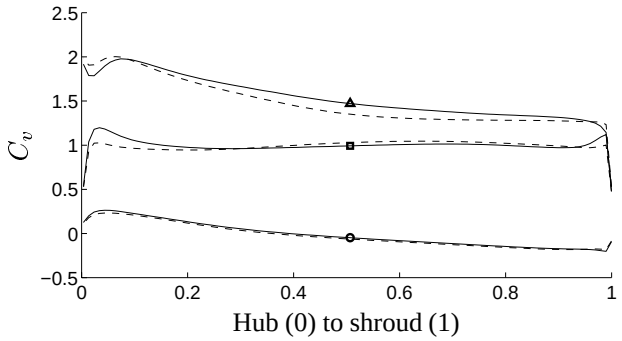

Figure 3.2: Velocity coefficient distributions above the runner blades. Solid lines: standard (with and without hub clearance); dashed lines: uniform inlet. Markers: △: tangential; □: meridional (axial); ○: radial.

flow is outward from the axis of rotation.

3.1 Guide vane computations

The main reason for computing the flow in the guide vane passage is to generate inlet boundary conditions for the runner computations. Comparisons with measurements show that the overall flow features in the guide vane passage are captured by the computations [13].

Figure 3.1 shows the computational results at the interface between the guide vane computations and the runner computations (see figure 2.3). The meridional velocity is defined as $C_m = \sqrt{C_r^2 + C_z^2}$. The effect of the curvature of the meridional contour can clearly be seen in the meridional velocity distribution, since it increases towards the shroud. The local increase in the meridional velocity close to the boundaries owes to boundary layer effects [9, 16]. The tangential velocity also increases towards the shroud, owing to the curvature of the meridional contour but, since the interface section is inclined, the conservation of angular momentum yields a larger tangential velocity at the smaller radius.

The inlet boundary condition has a non-negligible effect on the flow at the interface, especially in the boundary layers of the hub and shroud. It would therefore be interesting to make a thorough investigation of the flow in the spiral casing, but this is beyond the scope of this work.

3.2 Runner computations

The inlet boundary (see figure 2.3) conditions for the runner computations are taken from the circumferentially averaged guide vane computations (see figure 3.1). The inlet boundary conditions are constant in the circumferential direction. In reality, the flow at the inlet is influenced by non-uniform flow conditions and guide vane wakes, which makes the flow non-periodic and transient. The periodic and stationary approach used in this work, however, is believed to be sufficient for computations of the overall behaviour of the flow in the runner blade passages.

Three different runner computations are made. As a **standard** case, inlet boundary conditions from the 1/7 profile guide vane computations are used, and the hub clearance is *included*. As a **no hub clearance** case, inlet boundary conditions from the 1/7 profile guide vane computations are used, and the hub clearance is *excluded*. As a **uniform inlet** case, inlet boundary conditions from the uniform inlet guide vane computations are used, and the hub clearance is *included*.

Figure 3.2 shows the computed velocity distribution just above the runner blades (see figure 2.3). The meridional velocity is more uniform than at the interface between the guide vane and runner computations. Still, there are effects of the boundary layers at the boundaries, where the meridional velocity is increased locally [9, 16]. The conservation of angular momentum yields an increasing tangential velocity towards the smaller radius. There is a local reduction in the tangential velocity at the hub because of the upstream boundary layer interaction with the sudden change in wall rotation at the hub. The radial velocity ensures that continuity is fulfilled and that the flow is aligned with the meridional contour.

Figure 3.3 shows the angular momentum distribution at the runner inlet, at the section just above the blades, at section Ia and at section Ib (see figure 2.3). The hub-to-shroud abscissa is normalized with the channel width at each section. The angular momentum should be conserved in stream tubes where no power is extracted from the fluid [8, 11, 16]. Thus the change in angular momentum between the inlet and just above the runner blades and between sections Ia and Ib, respectively, reflects the quality of the computations (and measurements). It is found in ongoing work that insufficiently resolved grids or insufficient discretization schemes affect the conservation of angular momentum between the inlet section and the section just above the blades. In this case, there is is a small difference (see figure 3.3) , which is most likely an upstream effect of the runner blades, since the section just above the runner blades is very close to the runner blade leading edges. The grid resolution and discretization scheme above the blades are thus considered sufficient. The angular momentum distributions at Ia and

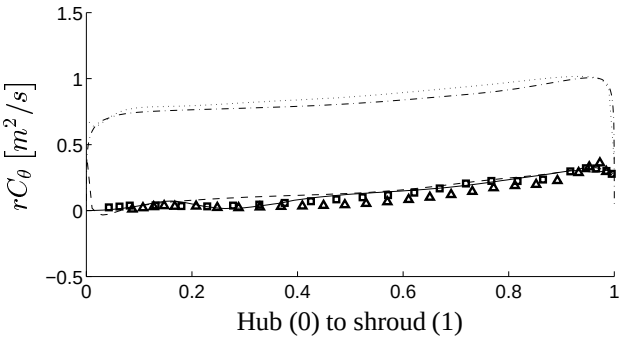

Figure 3.3: Angular momentum distributions. Dashed-dotted line: at the inlet of the runner computations; dotted line: just above the runner blades; dashed line: section Ia; solid line: section Ib. Measurement markers: □: section Ia; △: section Ib.

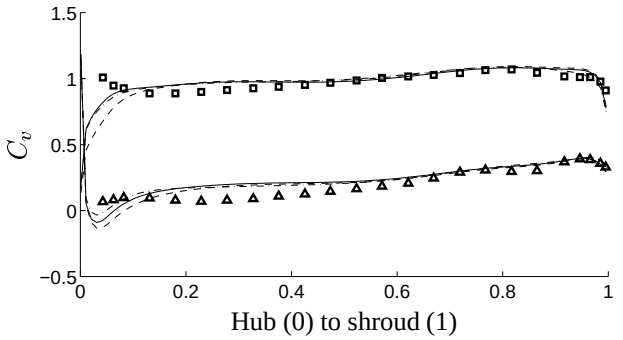

Figure 3.4: Velocity coefficient distributions at section Ia. Solid lines: standard; dashed lines: no hub clearance; dashed-dotted: uniform inlet. Measurement markers: △: tangential; □: meridional.

Ib are similar and compares well with the measurements made at *Turbine 99*. Note that the abscissas are normalized by the length at each section and that effects from the end of the hub cone are included at section Ib. The blade loading, which can be derived from the difference in angular momentum before and after the runner blades [8, 11, 16], seems to be quite uniform from hub to shroud.

Figure 3.4 shows the circumferentially averaged computed velocity distributions at section Ia (see figure 2.3). The velocity distributions are very similar to the *Turbine 99* measurements in the outer region (large radius), while they differ slightly from the measurements in the inner region. The main difference is the lack of a peak in the predicted meridional velocity close to the shroud. Andersson [2] argued that this peak originated in the leakage between the runner hub and the runner blades. A comparison between computations with and without the runner hub clearance shows that the hub clearance flow affects the flow but not to the extent that this peak is captured. While a comparison between different inlet conditions shows that the velocity profiles are more or less unaffected by the inlet condition, the meridional velocity at both the interface between the guide vane and runner computations (figure 3.1) and just above the blades (figure 3.2) has a peak close to the hub. This behaviour has been observed before [9, 16, 17], and measurements reveal that the effect can already be seen in the spiral casing [13]. The tangential velocity component in this region indicates a local reduction close to the hub, which can also be seen at section Ia. It seems that the peak in the meridional velocity is advected through the blade passage down to section Ia.

Examination of an iso-surface of large axial velocities shows that the advection of the meridional velocity peak is reasonable, and figure 3.5 shows that the peak is advected almost all the way through the blade passage. The reason for the disappearance of this peak at section Ia is most likely insufficient grid resolution after the runner blades, which should be studied. Figure 3.2 also shows that there are large axial velocities in the tip clearance but not in the hub clearance. This argues that the hub clearance flow is not responsible for the peak in the meridional velocity component, close to the hub at section Ia. The hub clearance is

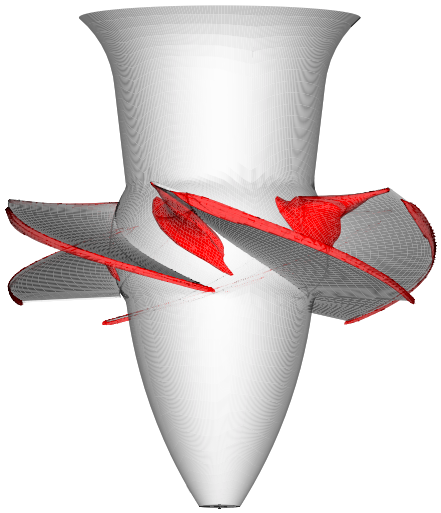

Figure 3.5: Isosurfaces of axial velocity. There are two regions of high axial velocity, one in the tip clearance and one on the suction side at the leading edge of the blades, particularly close to the hub.

not sufficiently resolved during the computations, however, which has a slight influence on the results in this region.

Despite the small influence of the inlet boundary condition on the flow at section Ia, it would be interesting to investigate the effects of the boundary layers in the spiral casing throughout the runner. This is however beyond the scope of this work.

Figure 3.6 shows the circumferentially averaged computed velocity distribution at section Ib (see figure 2.3). The computed flow features are comparable to that measured and presented at *Turbine 99* [1], and this is also included in the figure. However, the flow in the axial diffusor is very difficult to capture, especially close to the hub [17]. The flow at section Ib is also very dependent on the flow at section Ia, since computational errors are advected downstream. The periodic and steady assumptions also lack the same validity at section Ib, where there is a vortex rope formation with inherent instability, recirculation and streamline curvature caused by upstream effects of the draft tube bend. Experimental visualizations indicated a small recirculation region close to the rotational axis, and

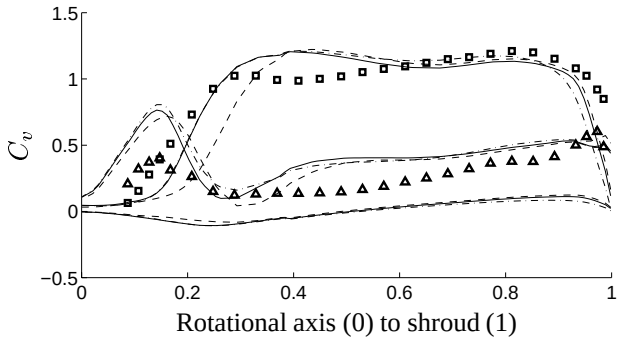

Figure 3.6: Velocity coefficient distributions at section Ib. Solid lines: standard; dashed lines: no hub clearance; dashed-dotted: uniform inlet. Measurement markers: △: tangential; □: meridional. The computed radial velocity is the one closest to zero.

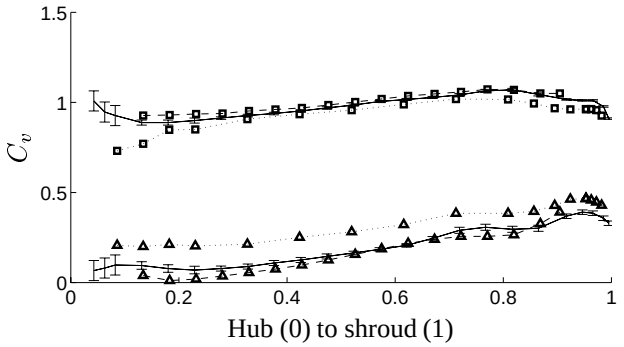

Figure 3.7: Comparison of three velocity measurements at section Ia. Solid lines: Ia(1); dashed lines: Ia(2); dotted lines: average of phase resolved measurements. Measurement markers: △: tangential; □: meridional. The solid lines have error bars that correspond to the estimated errors of the measurements.

both mean and RMS values of the velocity measurements as well as the visualizations indicated a vortex rope that extended to about $r^* = 0.25$ [2]. The figure shows the influence of the hub clearance and the inlet boundary condition. However, further studies of the flow in the axial diffusor must be done to be able to draw any conclusions from this figure.

It should be noted that the velocity measurements are more sensitive to minor changes in operating conditions than, for instance, overall efficiency and pressure recovery [3]. Furthermore, the velocity measurements at section Ia and section Ib, presented in figures 3.4 and 3.6, were made at a single tangential angle, which does not take into account the tangential variation. Figure 3.7 shows the three different measured velocity profiles of section Ia that were distributed at the time of the *Turbin 99 - II* workshop. Sections Ia(1) and Ia(2) are located at approximately opposite sides of the draft tube cone (section Ia(1) is the same as section Ia in the rest of the text). The measurements thus indicate a non-negligible tangential variation of 2% and 15% for the average of the meridional and tangential components, respectively [2]. The phase resolved measurements were made at section Ia(1) but at a slightly different operating condition, with about 1% lower mass flow owing to a plexiglass window failure. This gave a larger tangential velocity component and a lower meridional velocity component close to the hub, similar to the computations in this work.

Since the test head is not directly controlled (the speed of the main pumps is controlled), there was also a small drift in the operating condition during the measurement period that required compensation [3].

The error bars show that the three measurement points in section Ia(1) closest to the hub are very unreliable.

3.2.1 Radial velocity at section Ia

The radial velocity component at the inlet to the draft tube (section Ia, see figure 2.3) was not measured in the *Turbine 99* workshop. It was found during the workshop that the lack of the inlet radial velocity component and the different assumptions made by the contributors very seriously affected the computational results. Bergström [4] suggested that the velocity close to the walls at section Ia should be parallel to the walls. This assumption was selected as a standard for the *Turbine 99 - II* workshop. Bergström defined the radial velocity distribution as

$$u_r = u_{axial} \tan(\theta)$$

where u_r is the radial velocity and u_{axial} is the axial velocity. θ is the radial flow angle in the meridional plane and varies linearly between the hub and the shroud according to

$$\theta = \theta_{hub} + \frac{\theta_{shroud} - \theta_{hub}}{R_{shroud} - R_{hub}} (r - R_{hub})$$

$$R_{hub} \leq r \leq R_{shroud}$$

where $\theta_{hub} = -12.8^o$ and $\theta_{shroud} = 2.8^o$ at section Ia. The radius is defined by $r = \sqrt{x^2 + y^2}$. Figure 3.8 shows a comparison between the Bergström assumption and the radial velocity distribution computed for the standard case. This figure also gives a comparison showing the effect of the radial angle distribution on the radial velocity distribution using the computed axial velocity distribution and either a linear or the computed radial angle distribution. Figure 3.9 shows the computed radial flow angle at section Ia. It is more or less linear, as assumed by Bergström. The comparisons show that the computation and the assumption differ primarily close to the hub, where all the comparisons between computed and measured properties show that the computations fail slightly. Further studies must be done to quantitatively investigate the flow in this region.

3.2.2 Tip clearance flow

The runner blade tip clearance is included in all the computations in this work. Figure 3.10 shows some streamlines flowing through the tip clearance, in the region where the main formation of the tip vortex takes place. Figure 3.11 shows velocity vectors in a meridional cut through the center of the runner blade. The figure shows a zoom of the tip region. A swirling flow close to the tip on the suction side

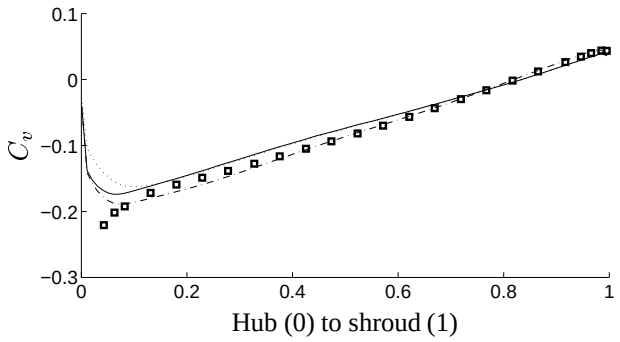

Figure 3.8: Radial velocity coefficient distribution at section Ia. Solid line: computed radial velocity distribution for the standard case; dashed-dotted: Bergström radial velocity approximation using the computed axial velocity and a linear radial flow angle; dotted lines: Bergström radial velocity approximation using the computed axial velocity and the computed radial flow angle. Markers: □: Bergström radial velocity approximation using the measured axial velocity and a linear radial flow angle.

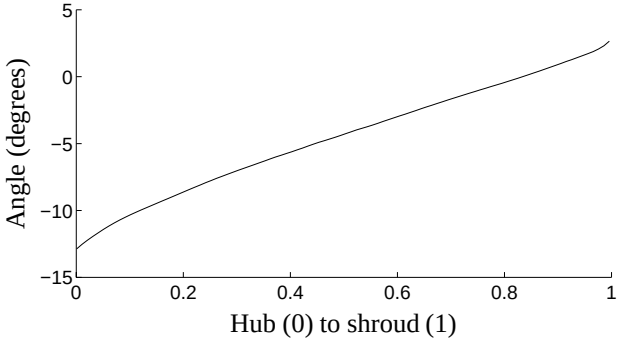

Figure 3.9: Computed radial flow angle distribution at section Ia.

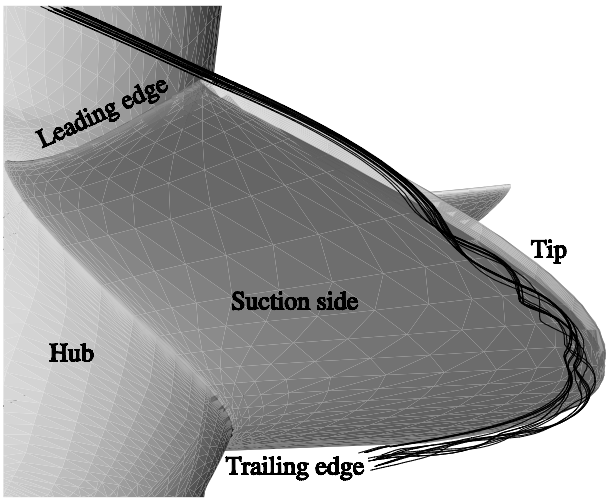

Figure 3.10: Tip clearance streamlines that form a tip vortex on the suction side of the blade.

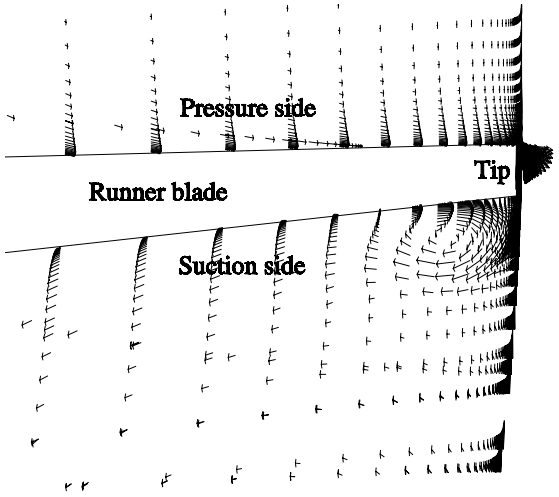

Figure 3.11: Velocity vectors in a meridional cut through the center of the runner blade, visualizing the tip vortex and other secondary flow features.

of the blade can clearly be seen. An essential technique for this kind of visualization of the tip vortex is to project the vectors in a plane that is orthogonal to the local blade angle (the main flow direction). This explains the strange-looking vectors in the shroud boundary layer. Furthermore, the secondary flow pattern shows a radial component outwards on the pressure side of the blade and a radial component inwards on the suction side of the blade. The radial flow on the pressure side can be explained by the increased importance of the centrifugal term in the boundary layer, where the magnitude of the velocity is decreased. The same analysis can be applied to the suction side, although here the boundary layer is very thin and cannot be seen in the figure. The radial flow inwards on the suction side of the blade comes from the scraping of the shroud boundary layer.

The computed volume flow through all five $0.4mm$-wide tip clearances is $5.45 \cdot 10^{-3} m^3/s$ for the standard case, which corresponds to 1% of the total volume flow, and $4.05 \cdot 10^{-3} m^3/s$ for the uniform inlet case, which corresponds to 0.8% of the total volume flow. Figure 3.12 shows that the tip clearance is widest at the leading edge. Figure 3.13 shows that the tip clearance flow is largest just before the width of the tip clearance is reduced to its minimum value. The flow features in the tip clearance are more or less independent of the inlet boundary condition, except for the magnitude of the axial velocity. The velocities are normalized by the volume flow and the representative section area at the center of the runner blade, $A_i = 0.14568 m^2$, where A_i is computed without runner blades. The maximum axial tip clearance velocity is thus roughly 2.5 times larger than the average axial velocity at this section.

3.2.3 Runner blade smearlines

The flow at the surfaces of the runner blades can be visualized by streamlines that are confined to a surface located at a small (constant) distance from the runner blade surface.

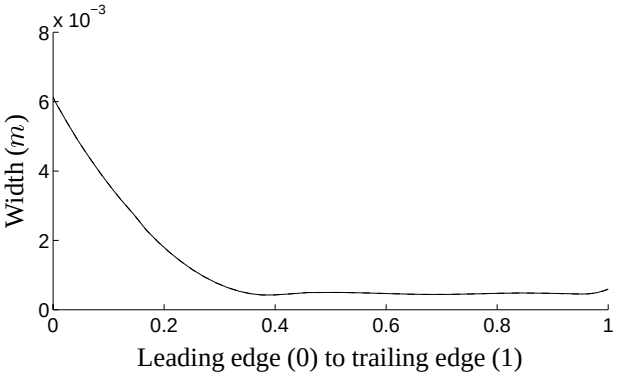

Figure 3.12: Tip clearance width distribution.

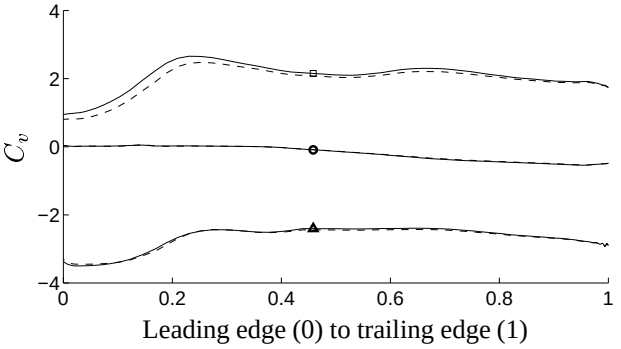

Figure 3.13: Tip clearance **relative** velocity coefficient distribution. Solid lines: standard; dashed lines: uniform inlet. Markers: △: tangential; □: meridional; ○: radial.

The equivalence in reality would be to follow the surface paths of oil drops that are moved by the flow close to the surface.

Figure 3.14 shows the smearlines of the pressure (a) and suction (b) sides of the runner blade. These smearlines are confined to the first grid plane in the flow, which is very close to the surface. The pressure side smearlines show that there is a flow component radially outwards, and that there is a stagnation line at the leading edge. The effects of the tip vortex can be seen close to the tip on the suction side. The radial velocity in the tip vortex is outwards close to the suction side surface, which gives the increased flow towards the tip that can be seen in the figure. The reattachment line of the tip vortex is located where the sudden change in radial velocity takes place. The width of the tip vortex thus increases from the leading edge to the trailing edge. The angle between the smearlines in the tip vortex region and the tip decreases from the leading edge to the trailing edge. This indicates that the tip vortex swirl intensity decreases along the blade, as the radial component becomes less significant.

The strange behaviour at the trailing edge of the suction side is most likely post-processing effects.

3.2.4 Runner blade wake

The runner blade boundary layers and the bluff runner blade trailing edge produce a wake after the runner blade. Figure 3.15 shows streamlines emitted from the vortex core

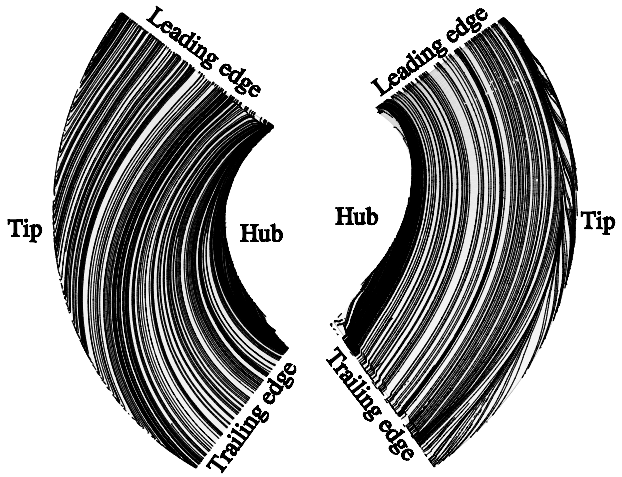

(a) Pressure side, top view. (b) Suction side, bottom view.

Figure 3.14: Smearlines following the flow very close to the runner blade surface.

after the trailing edge. The streamlines swirl about the vortex core before they escape into the main flow. The fluid close to the vortex core co-rotates with the runner blade, thus increasing the importance of the centrifugal term and yielding a radial component outwards in the core region.

The computations resolve a periodic behaviour of the wake at section Ia (see figure 2.3), as shown by Andersson [2]. However, it is important to have sufficiently small control volumes in the wake region. The computations are unable to predict the sharp wake peaks when the control volumes in the wake region are too large, yielding a more sinusoidal behavior (figure 3.16(a)). If the grid resolution in the wake region is refined, the wake is captured qualitatively (figure 3.16(b)). The measurements and the resolved computations show a distinct peak in the tangential velocity component in the wake region. The magnitude of the peak seems to be much greater in the measurements. However, phase averaging the measurements would yield results similar to those of the resolved computation.

3.2.5 Pressure recovery

At the *Turbine 99* workshop, Andersson [2] presented the pressure recovery of the draft tube from section Ia to the outlet of the draft tube. Figure 3.17 compares the computed pressure recovery for the standard case with the measured pressure recovery in the axial diffusor. The pressure recovery,

$$C_{Pr} = \frac{P_{wall} - P_{wall,Ia}}{P_{dyn,Ia}}$$

is normalized with the dynamic pressure at section Ia, $P_{dyn,Ia} = \rho Q^2/(2A_{Ia}^2) = 64.80hPa$ ($Q = 0.522m^3/s$, $A_{Ia} = 0.145m^2$, $\rho = 1000kg/m^3$). P_{wall} is the average of the measured pressure at two sides of the draft tube cone. For the computational results, P_{wall} is the circumferential

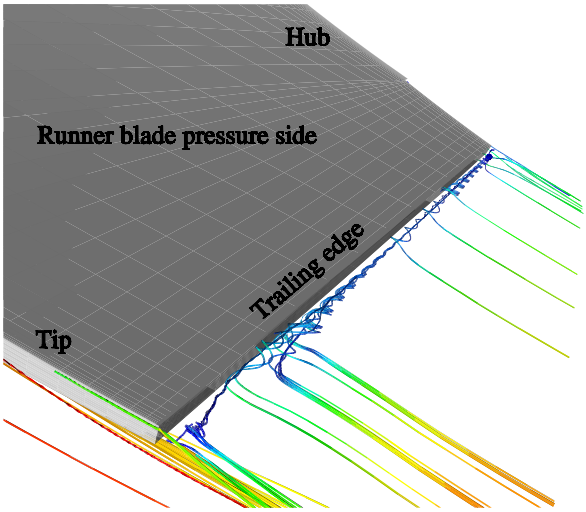

Figure 3.15: Streamlines emitted from the vortex core in the wake after the runner blade trailing edge.

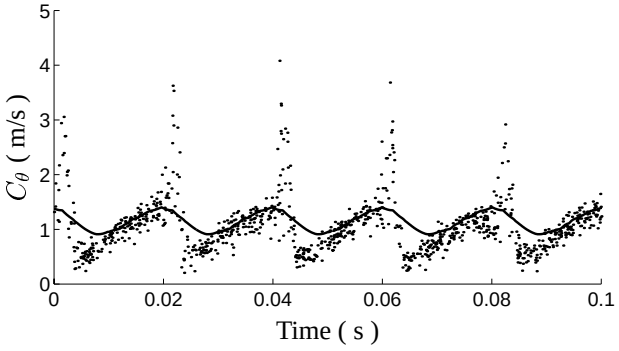

(a) Unresolved wake

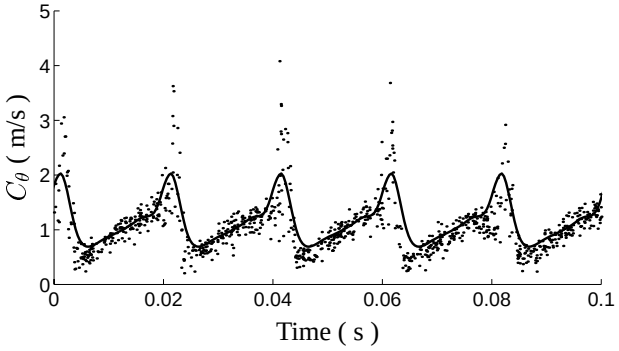

(b) Resolved wake

Figure 3.16: Comparison between computed and measured periodic behavior of the tangential velocity component at $r^* = r/R = 0.92$. Dots: individual measurement samples; solid line: computational results. The computational results have been phase-shifted to match the measurements because it was not able to obtain the exact runner angles of the measurements. One runner revolution (five blades passages) takes approximately 0.1s.

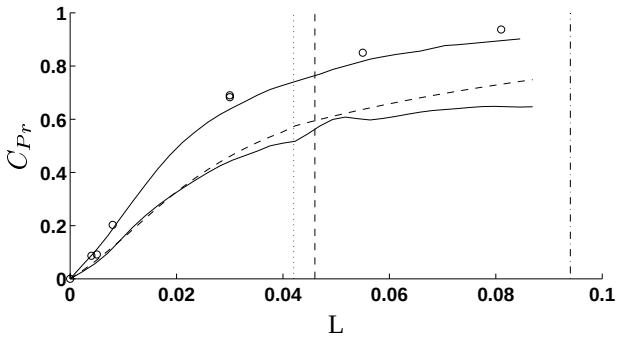

Figure 3.17: Comparison between computed and measured pressure recovery between section Ia and the end of the draft tube cone. ○: measured pressure coefficient; solid curve: computed pressure coefficient (top=wall, bottom=cross-sectional averaged); dashed curve: ideal pressure recovery. The vertical lines show some important locations: dotted line: end of runner cone; dashed-dotted line: section Ib; dashed line: end of draft tube cone. The abscissa, L, is 0 at section Ia and 1 at the end of the draft tube.

average of the pressure at the draft tube cone wall, since the computational domain is rotating. $P_{wall,Ia}$ is the corresponding value at section Ia. Andersson pointed out that most of the pressure recovery takes place in the very first part ($L < 0.6$) of the draft tube and that this pressure recovery is greater than an ideal one-dimensional assumption, defined by

$$C_{Pr,ideal} = 1 - \left(\frac{A_{Ia}}{A_i}\right)^2$$

where A_{Ia} is the area of section Ia and A_i is the area distribution along the main flow direction after section Ia. The computed pressure recovery, circumferentially averaged along the draft tube cone wall, agrees with the measurements. However, the cross-sectional averaged computed pressure recovery shows that the overall pressure recovery is slightly less effective than the ideal. Some small effects of the end of the hub cone may also be observed as a disturbance in the computed pressure recovery.

3.2.6 Integral values

Some of the integral values requested for the *Turbine 99* workskop were the flow rate

$$Q_{int} = \int_A U dA$$

the kinetic energy correction factor, axial component

$$\alpha_{axial} = \frac{1}{AU_{mean}^3} \int_A U^3 dA$$

the kinetic energy correction factor, tangential component

$$\alpha_{swirl} = \frac{1}{AU_{mean}^3} \int_A V^2 U dA$$

and the momentum correction factor

$$\beta = \frac{1}{AU_{mean}^2} \int_A U^2 dA$$

	Meas. Ia	Comp. Ia	Meas. Ib	Comp. Ib
Q_{int}/Q	0.96	1.00	1.03	1.00
α_{axial}	1.03	1.01	1.06	1.16
α_{swirl}	0.06	0.08	0.10	0.19
β	1.02	1.00	1.02	1.06

Table 3.1: Integral values.

where A is the area, U is the axial velocity component, V is the tangential velocity component and $U_{mean} = Q/A$ is the mean velocity at each section. The measured [2] and computed integral values at sections Ia and Ib are shown in table 3.1, where Q is the volume flow of the studied operating condition. The measured values are evaluated using linear interpolation between measurement points and linear extrapolation to the boundaries.

4 Conclusion

The computations presented in this work show good agreement with the experimental data presented at the *Turbine 99* workshop in 1999. The computational results show that the radial velocity profile assumption that was proposed for the *Turbine 99 - II* workshop is reasonable.

The discretization of the Hölleforsen turbine model was made using a complicated multiblock topology. The computations and the comparisons with the measurements reveal that this discretization should be improved. To capture the wakes after the runner blades, the grid resolution in this region must be increased.

The main differences between the computational results and the measurements are after the runner blades, close to the hub, where the computations fail to predict a peak in the axial velocity component. The computational results suggest that this peak originates in the boundary layers above the runner blades and not in hub clearance flow, as was argued at the *Turbine 99* workshop.

Future studies should improve the discretization in the region below the runner blades in order to be able to predict the periodic behaviour and the correct flow close to the hub.

Acknowledgements

This work is financed and supported by ELFORSK (Swedish Electrical Utilities Research and Development Company), the Swedish National Energy Administration and GE Energy (Sweden) AB.

Vattenfall Utveckling AB and its staff, particularly Urban Andersson and Rolf Karlsson, are gratefully acknowledged for their contribution.

GE Energy (Sweden) AB and its staff, particularly Bengt Nauclér, are gratefully acknowledged for geometrical information and support.

Computational resources at UNICC, Chalmers, is gratefully acknowledged.

References

[1] U. Andersson. An Experimental Study of the Flow in a Sharp-Heel Draft Tube. Thesis for the degree of Licentiate of Engineering 2000:08, ISSN: 1402 - 1757, Dept. of Mechanical Engineering, Division of Fluid Mechanics, Luleå University of Technology, 2000.

[2] U. Andersson. Turbine 99 - Experiments on draft tube flow (test case T). In *Proceedings from Turbine 99 - Workshop on Draft Tube Flow*, 2000, ISSN: 1402 - 1536.

[3] U. Andersson and R. Karlsson. Quality aspects of the Turbine 99 draft tube experiment. In *Proceedings from Turbine 99 - workshop on draft tube flow*, 2000, ISSN: 1402 - 1536.

[4] J. Bergström. Approximations of numerical errors and boundary conditions in a draft tube. In *Proceedings from Turbine 99 - Workshop on Draft Tube Flow*, 2000, ISSN: 1402 - 1536.

[5] L. Davidson. An introduction to turbulence models. Int.rep. 97/2, Thermo and Fluid Dynamics, Chalmers University of Technology, Gothenburg, 1997.

[6] L. Davidson and B. Farhanieh. CALC-BFC: A Finite-Volume Code Employing Collocated Variable Arrangement and Cartesian Velocity Components for Computation of Fluid Flow and Heat Transfer in Complex Three-Dimensional Geometries. Rept. 92/4, Thermo and Fluid Dynamics, Chalmers University of Technology, Gothenburg, 1992.

[7] J.P. Van Doormaal and G.D. Raithby. Enhancements of the SIMPLE method for predicting incompressible fluid flows. *Num. Heat Transfer*, 7:147–163, 1984.

[8] G. Krivchenko. *Hydraulic Machines: Turbines and Pumps, Second Edition*. CRC Press, 1994.

[9] T. Kubota. Normalization of flow profile data measured at runner inlet. In G. Sottas and I. L. Ryhming, editors, *3D-Computations of Incompressible Internal Flows - Proceedings of the GAMM Workshop at EPFL, September 1989, Lausanne - Notes on Numerical Fluid Mechanics*, pages 55–62. Vieweg, Braunschweig, 1993.

[10] P.K. Kundu. *Fluid Mechanics*. Academic Press, San Diego, California, 1990.

[11] B. Lakshminarayana. *Fluid Dynamics and Heat Transfer of Turbomachinery*. John Wiley & Sons, Inc., New York, 1996.

[12] H. Nilsson. A Numerical Investigation of the Turbulent Flow in a Kaplan Water Turbine Runner. Thesis for the degree of Licentiate of Engineering 99/5, Dept. of Thermo and Fluid Dynamics, Chalmers University of Technology, Gothenburg, 1999.

[13] H. Nilsson, U. Andersson, and S. Videhult. An experimental investigation of the flow in the spiral casing and distributor of the Hölleforsen Kaplan turbine model. Int.rep. 01/05, Dept. of Thermo and Fluid Dynamics, Chalmers University of Technology, Gothenburg, 2001.

[14] H. Nilsson, S. Dahlström, and L. Davidson. Parallel multiblock CFD computations applied to industrial cases. In C.B. Jenssen et al., editor, *Parallel Computational Fluid Dynamics - Trends and Applications*, pages 525–532. Elsevier Science B.V., 2001.

[15] H. Nilsson and L. Davidson. CALC-PVM: A parallel SIMPLEC multiblock solver for turbulent flow in complex domains. Int.rep. 98/12, Dept. of Thermo and Fluid Dynamics, Chalmers University of Technology, Gothenburg, 1998.

[16] H. Nilsson and L. Davidson. A numerical comparison of four operating conditions in a Kaplan water turbine, focusing on tip clearance flow. In *Proceedings of the 20th IAHR Symposium, Hydraulic Machinery and Cavitation*, 2000.

[17] H. Nilsson and L. Davidson. A validation of parallel multiblock CFD against the GAMM Francis water turbine runner at best efficiency and off-design operating conditions. Int.rep. 01/02, Dept. of Thermo and Fluid Dynamics, Chalmers University of Technology, Gothenburg, 2001.

[18] D.C. Wilcox. Reassessment of the scale-determining equation for advanced turbulence models. *AIAA J.*, 26(11):1299–1310, 1988.